

Microstructure analysis of TIG welded additively manufactured prepared joints of Ni-based superalloys produced by Laser Powder Bed Fusion

Ole Geisen, PhD¹, Tad Steinberg²

¹ Siemens Gas and Power GmbH & Co. KG, Berlin, Germany

² Siemens Energy Inc, Orlando Innovation Center, Orlando, Florida

ABSTRACT

Laser powder bed fusion (L-PBF) of entire assemblies is not typically practical for technical and economic reasons. The build size limitations and high production costs of L-PBF make it competitive for smaller, highly complex components, while the less complex elements of an assembly are manufactured conventionally. This leads to scenarios that use L-PBF only where it's beneficial and requires integration and joining to form the final product. Today the welding process requires complex welding fixtures and tack welds to ensure correct alignment and positioning of parts for repeatable results. In this paper, both L-PBF and milled weld preparations are presented to simplify Tungsten inert gas (TIG) welding of rotationally symmetrical geometries using integrated features for alignment and fixation. All welds produced in this study passed the highest evaluation group B according to DIN 5817.

Citation: Ole Geisen, Tad Steinberg, "Microstructure analysis of TIG welded additively manufactured prepared joints of Ni-based superalloys produced by Laser Powder Bed Fusion," In *Proceedings of the Ground Vehicle Systems Engineering and Technology Symposium (GVSETS)*, NDIA, Novi, MI, Aug. 16-18, 2022.

1. Introduction

Laser powder bed fusion (L-PBF) is one of the most mature additive manufacturing (AM) technologies today, with applications in the aerospace, medical, and energy sectors, among others [1]. One of the main advantages of L-PBF is the design freedom that enables the manufacture of highly complex geometries [2]. When these complex L-PBF-manufactured components are integrated into a larger assembly that

requires substance-to-substance bonds, appropriate joining methods and setups need to be determined.

The focus of this study is on a combination scenario: joining highly complex L-PBF-built swirlers to milled manifolds to form the combustion system of an SGT-8000H Siemens Energy gas turbine, as shown in Figure 1. The material used for both the swirlers and the manifold in serial production is Inconel 625 (IN625); Tungsten inert gas (TIG) welding is used as the joining technology.

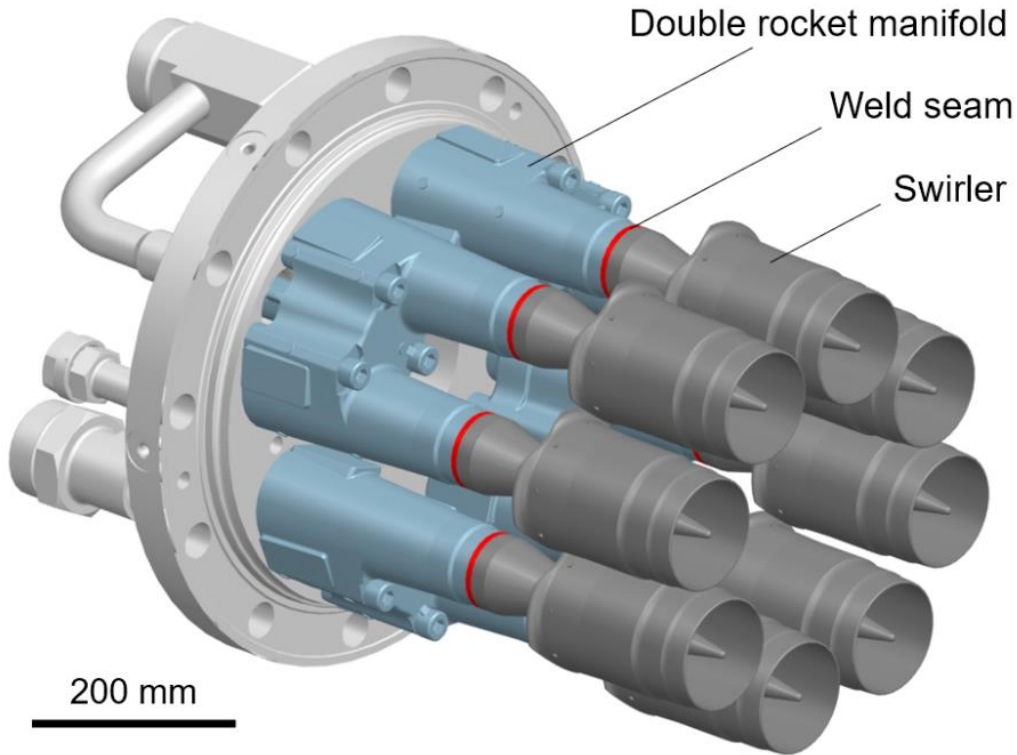


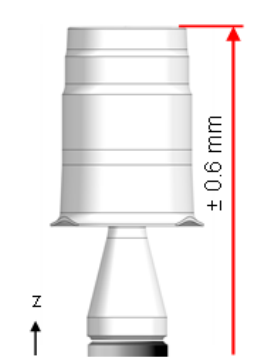


Figure 1: SGT-8000(H) combustion system with weld seams between swirlers and manifolds highlighted in red

The geometric accuracy of the weld assembly is critical to the performance of the combustion system. The positioning of the swirlers entails a centering, a rotational alignment, and an axial distancing, as illustrated in Table 1. For prototypes or components with low production volumes, this is commonly achieved with manual

alignment. In serial production, part-specific fixtures are often used for improved productivity and reproducibility. After the positioning, standard welding process chains usually include tack welding operations, which are necessary for preliminary fixation of the components before the actual weld seams are set.

Table 1: Swirler positioning.

1.1 Centering	1.2 Angular alignment	1.3 Axial distance
 <p data-bbox="359 1910 550 1944">In flow direction</p>	 <p data-bbox="665 1910 917 1944">Against flow direction</p>	 <p data-bbox="971 1910 1085 1944">Side view</p>

The goal of this study was to tap the potentials of L-PBF to eliminate the need for fixtures and to simplify the welding-related process chain by developing and testing novel weld preparation designs to fulfilling the following tasks:

2. The state of the art

Research on the welding of materials produced with L-PBF is covered in numerous studies, for example by Wits et al. [3], Casalino et al. [4] and Mäkikangas et al. [5]. The joining of machined and as-built L-PBF tubes from Ni-based superalloys IN625 and IN718 via laser beam was investigated by Jokisch et al. [6]. While the weldability was generally shown, some as-built L-PBF weld edges included agglomerations of silicate-like inclusions. In contrast, machined weld edges had a shiny surface with no inclusions, indicating an influence of the L-PBF surface on the welding. Geisen et al. [7] successfully joined L-PBF-manufactured tubes from IN625 and IN718 via TIG welding. All specimens were machined to a V-seam weld preparation, and no as-built edges were welded. Unlike Jokisch et al., the authors did not discover significant defects.

One of the key advantages of AM is the ability to integrate additional functions and features into the design without increasing manufacturing costs. This feature can be used to improve assembly setups. For example, Klahn et al. [8] and Ramírez [9] investigated the integration of snap-fit joints to simplify the assembly of polymeric AM components. The standard ISO/ASTM 52910 [10] also states that AM can yield great potential when assembly features are included in AM components. ISO/ASTM 52911-2 [11] names specific AM geometries like hooks and threads to connect components.

3. Materials and methods

The base material for both the L-PBF and the conventional specimens was Inconel 625

1. Part positioning
 - a. Centering
 - b. Rotation
 - c. Axial distance

2. Part fixation

The motivation for the research of Fieger et al. [12] into joining L-PBF and materials conventionally manufactured from steel was the restricted build volume of L-PBF machines and the higher efficiency using L-PBF for the manufacture of small and medium-sized parts compared with large parts. While the design advantages of AM components can offer benefits for part assembly, little research has been done in the field of welding-related AM designs. Schwarz et al. [13] studied the welding of wrought and L-PBF stainless-steel 316L with TIG and laser beam welding. To improve the welding process, they developed L-PBF weld joint geometries for thin-walled metal sheets. The geometries include an integrated weld joint backing and geometrical features for the positioning of specimens. While this improved the welding process, clamping and tack welding of the specimens was still required. In addition, the geometries were not developed or tested for circumferential weld seams.

The following investigation will address this research gap. Based on the swirler use case, the focus will be on circumferential weld joints of IN625 parts and TIG welding. The targeted designs need to cover the above-mentioned main tasks (centering, rotation, axial distancing, and part fixation) while respecting both L-PBF and milling constraints. The part assembly before welding will be analyzed, followed by a validation of the seam quality and the geometric accuracy. Finally, the applicability of the results to other use cases and industries will be discussed.

(IN625), a high temperature-resistant Nickel-base superalloy commonly used in gas turbine combustion systems. Thermanit 625 (UTP A 6222 Mo) was used as filler

material. It's designed for weld joints of similar high-strength and highly corrosion-

resistant Nickel-based alloys [14, 15]. The compositions are listed in Table 2.

Table 2: Chemical compositions of Inconel 625 (powder and milled tube) and of the filler material Thermanit 625 in weight-percent (wt.%)

	Ni	Cr	Fe	Mo	Nb + Ta	C	Mn, Si	Si	P, S	Co	Al, Ti
Inconel 625	Bal.	20.0-23.0	≤ 5.0	8.0-10.0	3.15-4.15	≤ 0.1	≤ 0.5	≤ 0.5	≤ 0.015	≤ 1.0	≤ 0.4
Thermanit 625	Bal.	22	< 0.5	9	3.6	0.03	0.2	0.25	-	-	-

The L-PBF specimens were produced with IN625 powder from EOS GmbH on an EOS M290 using standard process parameters with a layer thickness of 40 μm from EOS GmbH. All L-PBF specimens were solution-annealed and grid-blasted with silicon carbide. The milling was performed on a five-axis CNC milling center (Alzmetall GS800) using Siemens NX CAM software for programming. The milled specimens were machined from sections of semi-

finished IN625 pipes with a diameter of 48.3 mm and a wall thickness of 3.68 mm, providing about 0.3 of machining stock. The final specimen geometries are shown in Figure 2. The L-PBF and milled pipe specimens had a length of 75 mm, a diameter of 48 mm, and a wall thickness of 3.4 mm. Orientation features (OF) were added on the outer diameter of the pipe specimens to provide planes for referencing the 3D scanned parts.

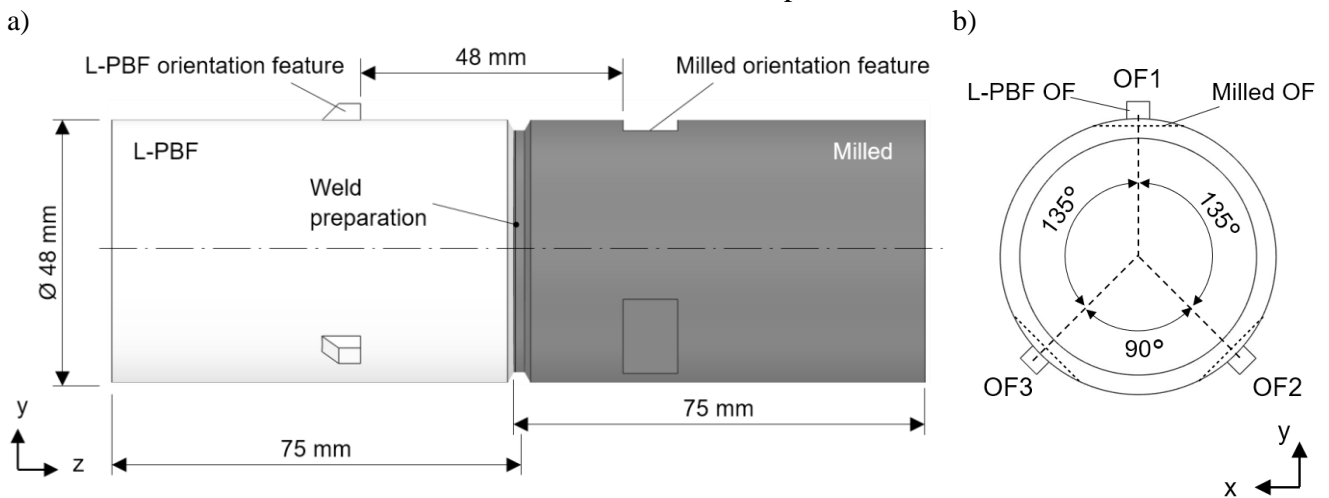


Figure 2: Specimen geometry: a) side view, b) front view of an assembled pair of welding pipes with positions of the orientation features (OF) used in all designs.

Optical blue light scans (3D scans) were performed with an ATOS 5 optical metrology system (GOM GmbH). The software GOM Inspect Professional was used to analyze and evaluate the scan data.

TIG welding was performed on a Polysoude CNC welding lathe (see Figure 3b). The assembled probe was clamped on the milled specimen, with continuous gas feeding on the inside.

a)

b)

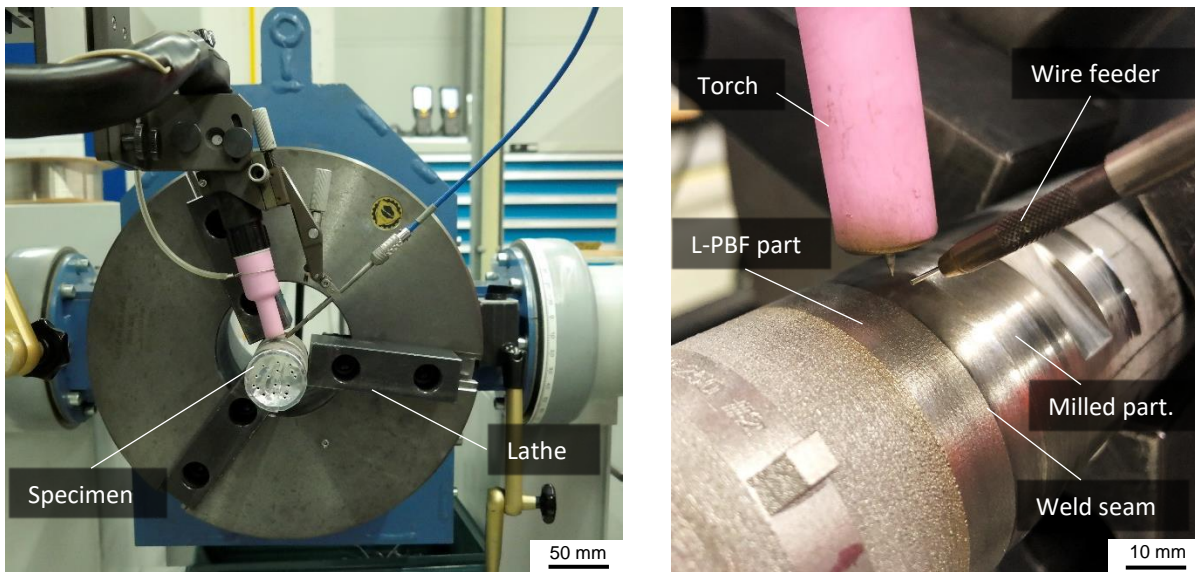


Figure 3: Polysoude orbital TIG welding station with (a) view of the welding lathe and (b) detailed view of the torch with the Tungsten electrode (left) and Thermanit 625 wire (right)

Argon (grade 4.6) with a flow rate of 10 l/min was used for purging and forming.

The parameters of the root and cover layer are listed in Table 3. The specimens were assembled manually without tack welds. No fixtures

(shown in **Error! Reference source not found.b**)) are listed in

were used for alignment and fixation prior to and during welding.

Table 3: Welding parameters for root and cover layer

Parameter	Root pass	Cover pass
Current type	Direct current	Direct current
Voltage	8.8 V	9.0 V
Peak current	94 A	64 A
Base current	47 A	24 A
Peak current interval	170 ms	170 ms
Base current interval	70 ms	70 ms
Rotation speed	70 mm/min	85 mm/min
Wire feed	600 mm/min	250 mm/min

The metallographic cuts of the weld seams were produced with a final polish using 3 μm diamond paste to expose the microstructure and detect pores and cracks. The cuts were electrochemically etched with Kalling's II etchant. Light optical microscopy (LOM)

was conducted using a Zeiss Axio Imager A2m microscope. An electron backscatter diffraction (EBSD) analysis was conducted using a Zeiss Sigma REM System equipped with a Bruker X-Flash EBSD detector.

4. Weld preparation designs

In this study, two different weld preparation designs were developed. The designs are based on the standard joint geometry depicted in **Error! Reference source not**

found.a) The butt joint of the standard setup allows an axial distance to be defined, but centering, rotation, and fixation are not covered. Both designs developed in this study have an additional circumferential wall for centering, as shown in **Error! Reference source not found..**

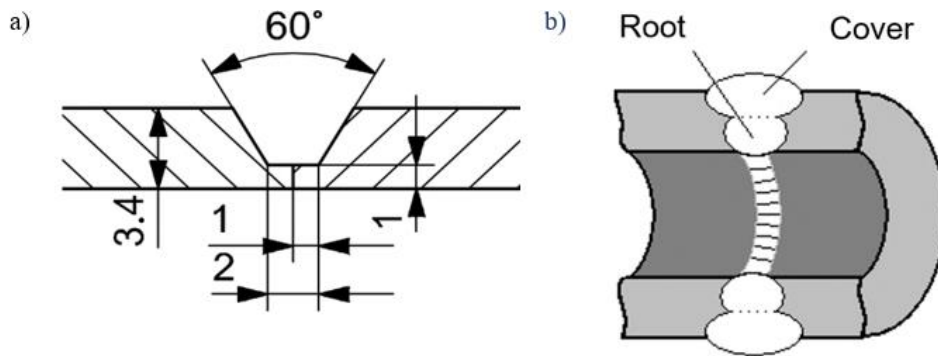


Figure 4: a) Standard weld preparation geometry, b) root and cover pass

The features for limiting the radial and axial movement after assembly need to fit into the design space and meet the manufacturing requirements: Standard L-PBF design rules on overhangs (45°) and minimum wall

thickness (0.3 mm) apply, while the milling is performed using standard tools with a minimum groove width of 0.2 mm, as illustrated in **Error! Reference source not found..**

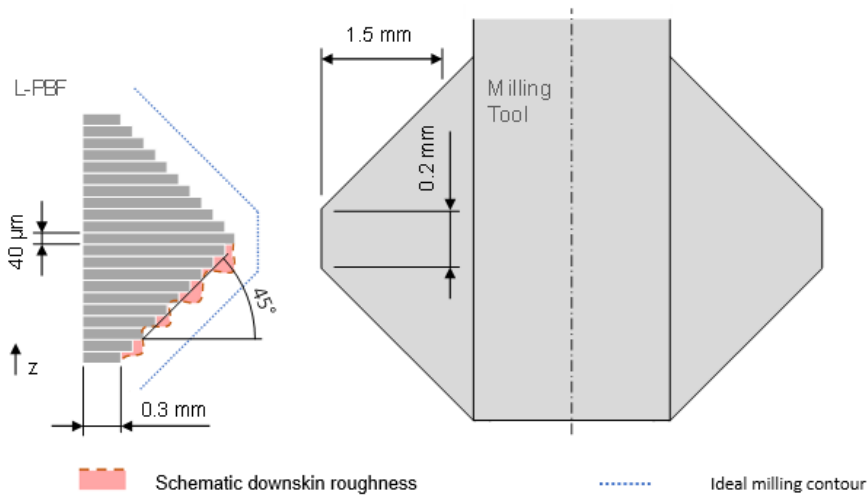


Figure 5: Geometric constraints for a) L-PBF with a layer thickness of $40\ \mu\text{m}$, allowable overhang of 45° , min. wall thickness of 0.3 mm; b) milling tool with a groove width of 0.2 mm, chamfer of 45° , max. depth of 1.5 mm; dimensions not to scale

4.1 Snap-fit design

The snap-fit design includes complementary tongue-groove geometries for the rotational alignment: A cut-out in the wall on the milled side (“groove”) is complemented by a

protrusion (“tongue”) on the L-PBF geometry. **Error! Reference source not found.b)** shows details of the L-PBF and the milling design in CAD. The axial fixation uses snap-fit pins that are integrated in the L-PBF weld preparation. Gaps between the pins and the circumferential walls allow the

pins to deflect during assembly. The pins and the milled slots create an interlocking fixation.

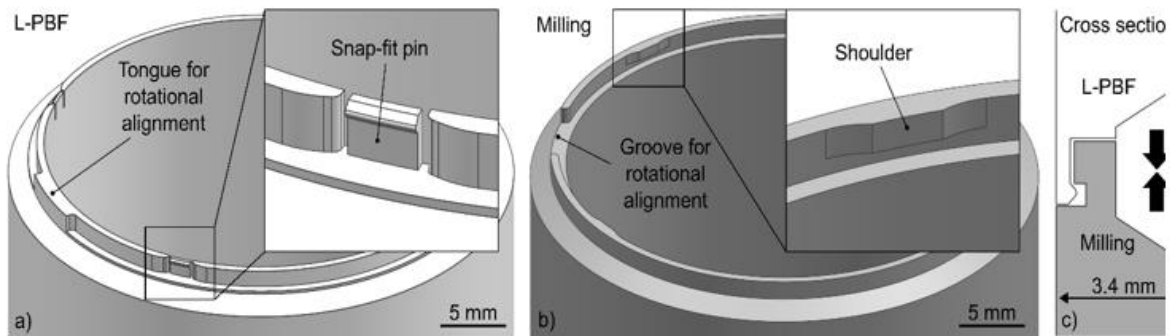


Figure 6: Snap-fit design with a) L-PBF geometry with tongue and pin, b) milling geometry with groove and shoulder, c) schematic assembly design

4.2 Bayonet Design

The bayonet design includes bayonet mount features for part fixation, as illustrated in **Error! Reference source not found.**. After plugging both sides together, the parts need to be twisted to interlock the bayonet geometries. Integrated end-stop surfaces

stop the rotation at a defined angle to ensure the correct rotational alignment. The L-PBF down skin surface and the corresponding milled surface have an overhang angle of 45° to enable support-free manufacturing via L-PBF. A standard milling tool as shown in **Error! Reference source not found.** is used to create the V-shaped bayonet feature.

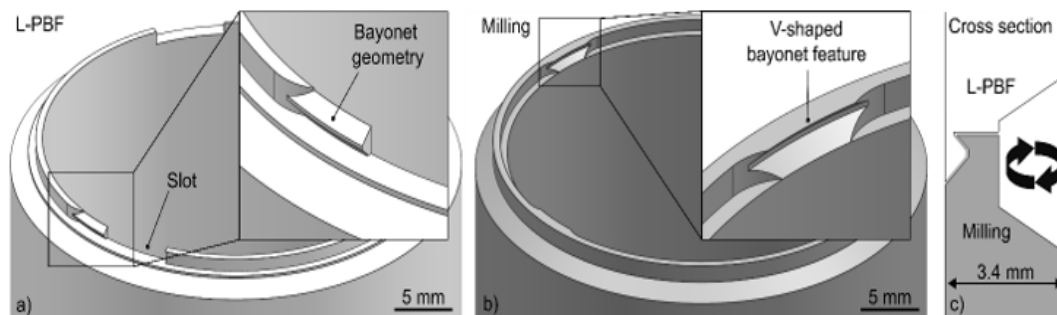


Figure 7: Bayonet design with a) L-PBF geometry (male), b) milling geometry (female), c) schematic assembly design

5. Results and discussion

5.1 L-PBF results

Close-ups of the L-PBF specimens with the corresponding CAD models are shown in Figure 4. The parts were built with no interruptions, and the alignment features show the expected resolution. No difference in L-PBF production cost and lead time was

observed, because the total number of layers remained unchanged with only minor changes in total part volume. The L-PBF specimens were not machined. As is common with L-PBF components, the down skin surfaces showed a higher surface roughness (compare [16]). While this can increase friction and require additional effort during assembly, the same effect can improve the fixation by preventing the parts from untwisting and unintentional disassembly.

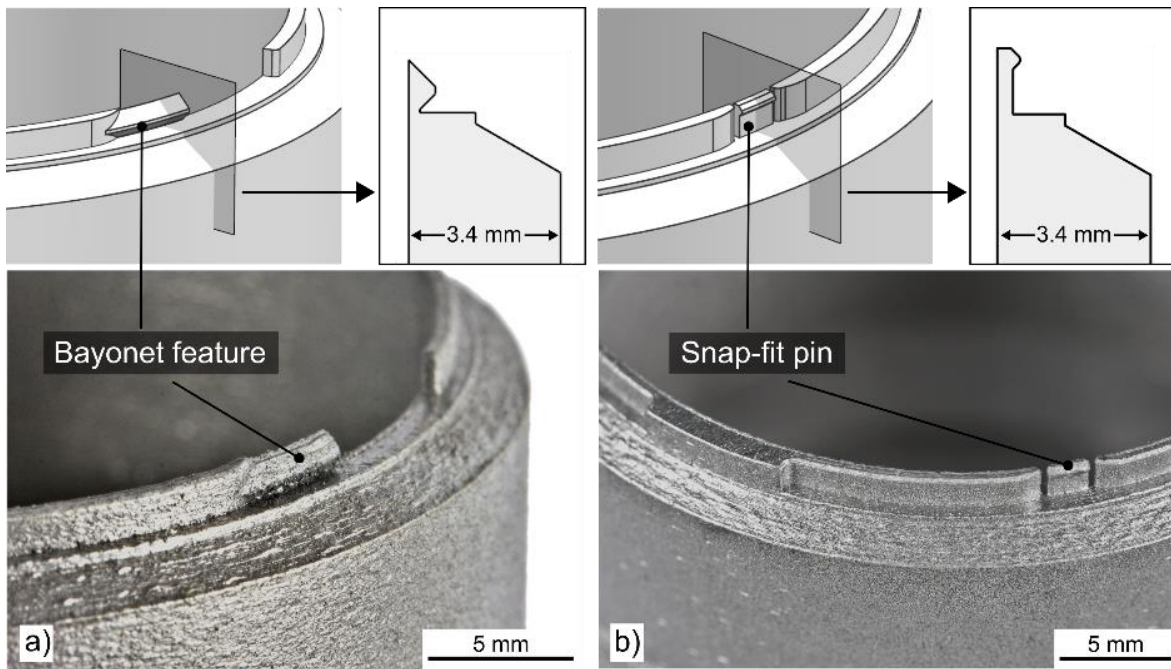


Figure 4: Close-up images of L-PBF specimens with a) snap-fit features and b) bayonet features

Irregularities were found on several thin-walled snap-fit pins. They showed bulky material accumulation and deformed pin walls. All affected pins were positioned in parallel to the steel recoater blade during the build job, and the material accumulations were only observed in the recoating direction, as shown in Figure 5. All of the pins that were not positioned in parallel to

the recoater were manufactured without errors. It is therefore likely that the defects were caused by contact with the recoater blade, with the wall thickness of 0.35 mm proving too low to withstand the forces occurring during the recoating process. The fixation function of the damaged pins is likely to be limited, and the affected parts are therefore discarded.

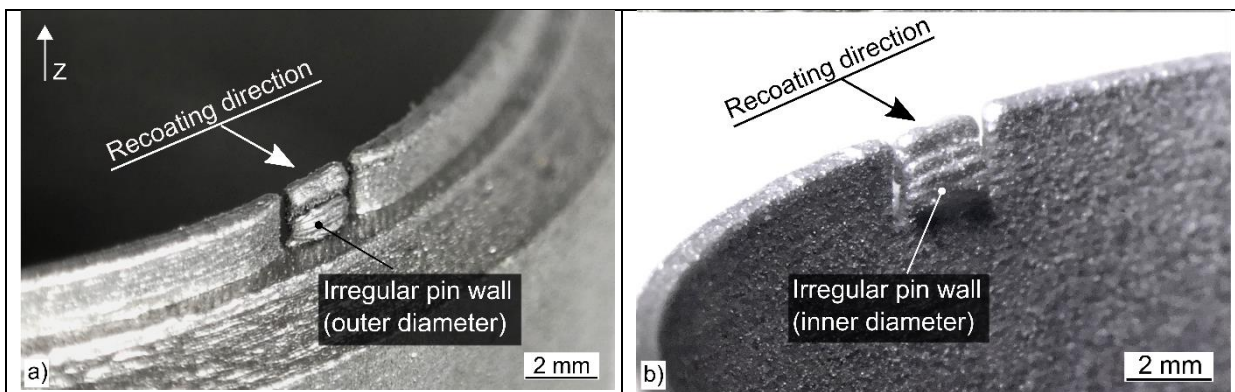


Figure 5: Deformed snap-fit pins a) on the outer diameter, b) on the inner diameter, with recoating direction

The metallographic cuts of the unwelded specimens in Figure 9a) and c) show cross-sections of the fixation features for axial fixation. Some individual pores were detected in the L-PBF specimens, especially

in the near-surface area, which is common for L-PBF [17]. All the pores were within the acceptance levels of the swirler, and no defects like cracks or lack of fusion were observed.

5.2 Milling results

Figure 6 shows close-up views of the milled weld joint preparations. No significant errors or irregularities were observed. The increased complexity of the developed designs compared with the state-of-the-art

geometry resulted in an increase in milling lead time for the weld preparation of about 30 percent for both designs. The milled geometries can be produced with commercially available, non-customized milling tools, making the designs also suitable for serial production.

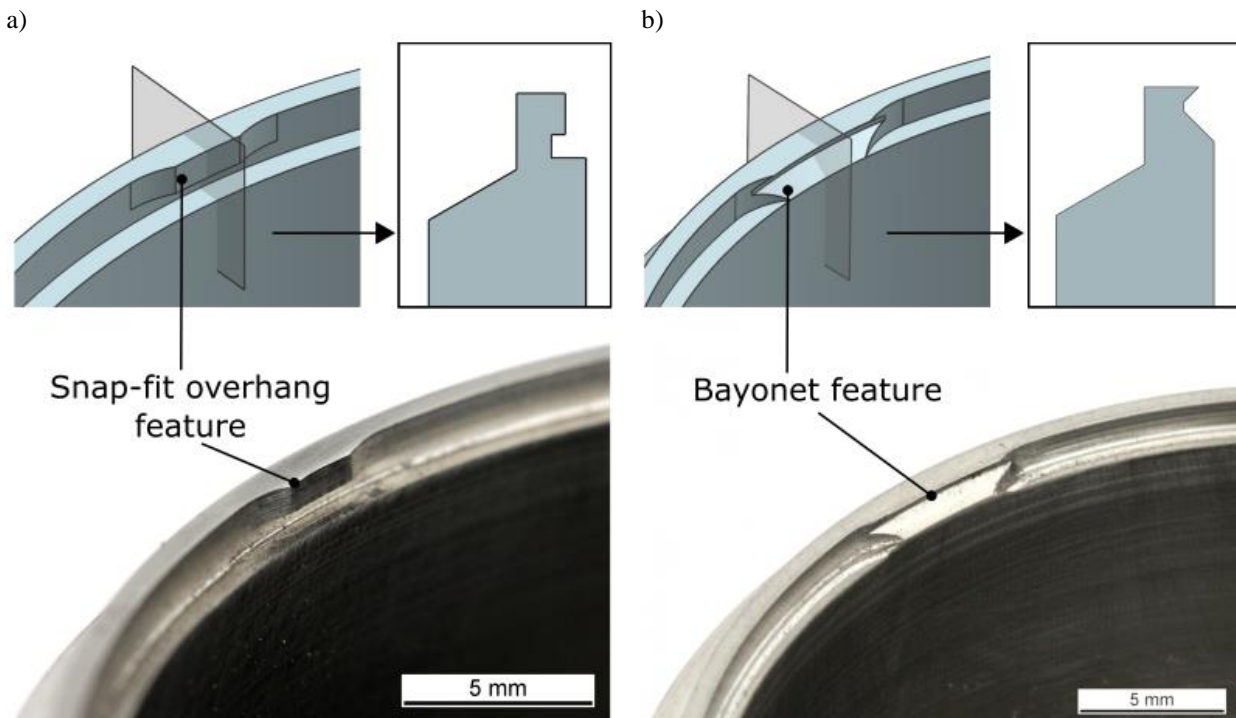


Figure 6: Close-up images of milled specimens with a) snap-fit features and b) bayonet features

5.3 Fixation capability

For the assembly, specimens of the bayonet mount had to be plugged together and then twisted. During the first assembly operation, high resistance to the twisting was observed. The bending of the bayonet geometry (see Figure 9c) was likely caused in the first assembly due to a tight part fit of the joint. With repeating assemblies, a constant fit was obtained. After assembly, it was not possible to separate the specimens under manually applied axial or radial loads that imitated rough shop-floor handling.

The snap-fit design is assembled by pushing the specimens together axially. This assembly required significantly less force

than the bayonet design. It was possible to manually disconnect specimens by applying an axial force. The snap-fit pins appeared to deform plastically with every assembly iteration: After more than five assemblies, the interlocking became too weak to hold the specimen's dead weight. Reliable handling and subsequent repeatable welding results therefore can't be guaranteed when the parts are disassembled multiple times.

Overall, the bayonet design creates a stronger fixation. The handling of assembled components is considered safer with the bayonet. The bayonet could be suitable for heavier components and therefore for a

wider range of potential use cases. The assembly and handling appeared to be stable and repeatable, potentially reducing non-

conformance costs and improving cycle times in production.

5.4 Geometrical alignment before welding

Four pairs of assembled specimens of each design were 3D scanned in horizontal position before welding. Gravity would therefore expose any allowance or gap between the assembled specimens, resulting in a mismatch of the center lines (as can be seen in Figure 11c). The orientation features on the specimens were used for reference.

The axial distance of the orientation features was 48.14 mm on average (48 mm target distance). The shortest distance was 47.97 mm, and the maximum distance was 48.33 mm. The results indicate good geometrical accuracy of the joints with deviations within the acceptable limits for the swirler use case (± 0.6 mm).

The average angular deviation was measured to analyze the rotational alignment of the specimens. On average, the deviation was 0.37° . Negative values for the bayonet design indicate that the specimens were not twisted far enough. The highest absolute deviation of -1.14° was measured on a bayonet specimen. Its assembly showed resistance to twisting due to a tight part fit,

which was likely the cause of the angular deviation.

The centering of the cylinders was analyzed by measuring the position deviation of the L-PBF center lines relative to the center line of the milled specimen. Selected 3D scan results are depicted in Figure 11. The center lines of the bayonet design are almost parallel to the target, with low absolute deviations as shown in Figure 11b). The 3D scans of the snap-fit design showed a sagging of the L-PBF cylinder in the direction of gravity, resulting in a sloping L-PBF center line (see Figure 11a). The cylinder sagging confirms the results of the assembly tests, where a weaker fixation of the snap-fit compared with the bayonet was observed. The average centering deviation of all the snap-fit specimens was 0.70 mm, and the average deviation of the bayonet specimens was 0.28 mm. Only the bayonet design therefore enables an assembly that meets the positioning accuracy required for the component after welding

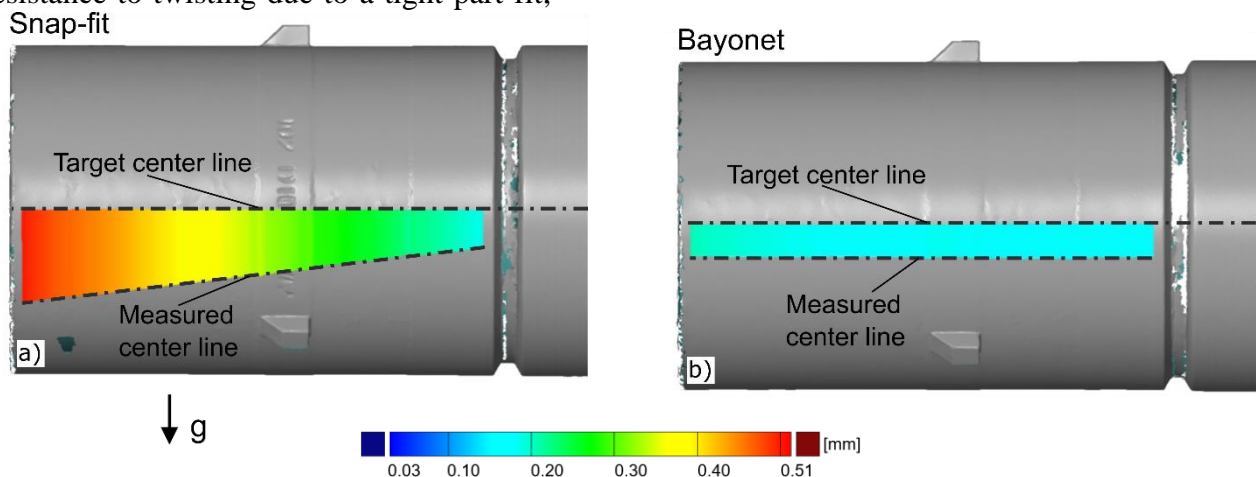


Figure 7: 3D scan results before welding of a) snap-fit and b) bayonet design with measured center lines of the L-PBF cylinders relative to the target center lines: A scaling factor of 30 was applied to improve visibility.

5.5 Geometrical alignment after welding

Weld shrinkage led to a reduced axial distance and overall length of the specimens. This resulted in an average orientation feature distance of 47.30 mm after welding. The shrinkage was relatively constant, with a variation of approximately ± 0.20 mm over all the samples, and it can therefore be easily compensated by systematically increasing the part length. A higher shrinkage of the L-PBF parts, as reported by Schwarz et al. [13], was not observed. The welding had no negative impact on the angular alignment, with comparable results before and after welding.

However, an impact on the center line mismatch was observed, as shown in two examples Figure 11. Both cases show a slight torsion of the cylinders, with a maximum radial center line deviation of 0.5 mm for the snap-fit and 0.4 mm for the bayonet design. While at 0.7 mm the average deviation of the snap-fit specimens is — similar to the results before welding, the average deviation of the bayonet design increases by a factor of 2.4. The deformation direction relative to the starting point of the circumferential weld showed a uniform trend

over all designs, as seen in the examples in Figure 11. The mechanical fixation of all parts remained intact during welding and led to acceptable welding results: While most of the welded parts met the centering requirement of 0.5 mm defined for the swirlers, the deviations were all within the process window of heat straightening. The maximum deviation observed was 1.03 mm. As a welding correction process, heat straightening is a standard step in the production of combustion systems today when using fixture. However, researchers should determine whether the precise alignment of the bayonet design after assembly can be preserved by adding tack welds before the circumferential welding. To summarize, the proposed fixture-less designs perform as well as or better than the current design with fixtures, while enabling significant time savings during weld preparation, because part alignment and tack-welding are not required. Eliminating the dependency on part-specific fixtures is an additional advantage that can increase production flexibility.

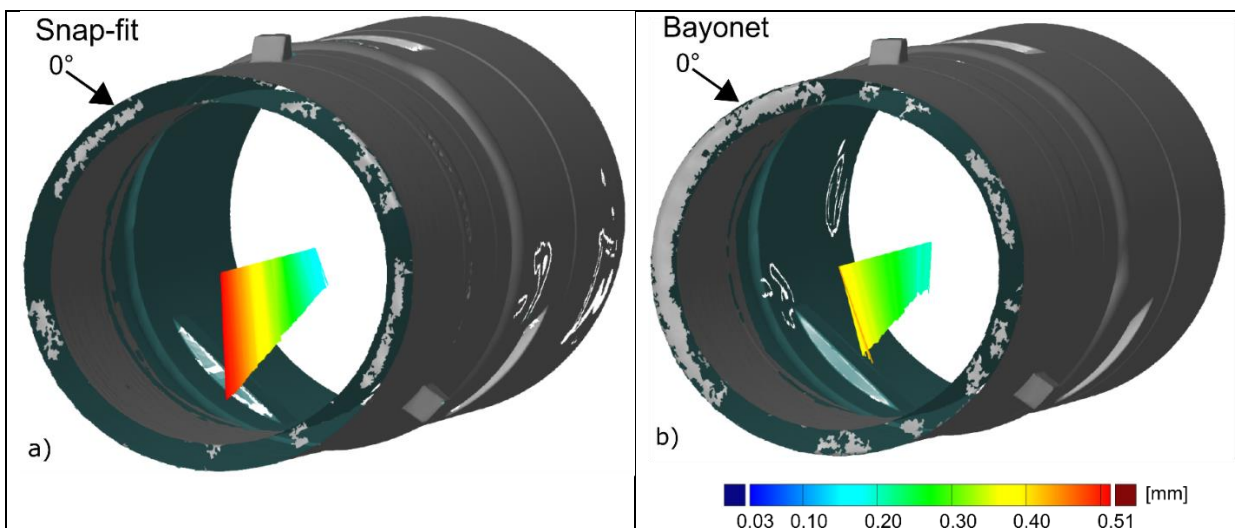


Figure 8: 3D scan results after welding of a) snap-fit design and b) bayonet design with measured center lines of the L-PBF cylinders relative to the target center lines. A scaling factor of 30 for these deviations was used to improve visibility. 0° indicates the starting position of the root weld

5.6 Weld joint analysis

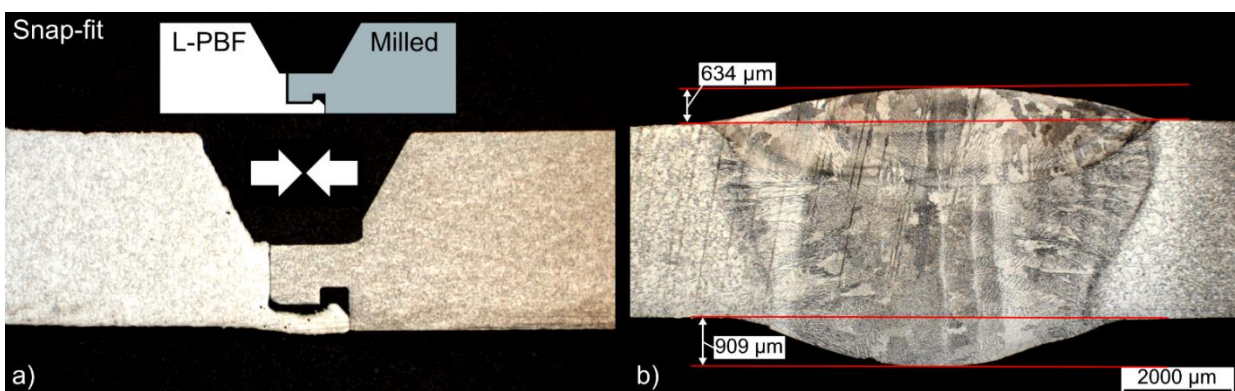
The weld seams were analyzed using evaluation criteria from DIN EN ISO 5817 [18]. The goal was to achieve quality level B for all welds, which is the required classification for most weld seams in gas turbine manufacturing.

In the visual inspections, no weld seam showed external defects like macro cracks or open pores on the surfaces. Uniform and circularly textured weld beads were formed on the cover layer. Even though the weld preparations were not machined and pores were observed under the L-PBF surface, no inclusions or other defects on the weld surface were present, as were found in the study of Jokisch et al. [6]. The quality of the welds is comparable to the results of Geisen et al. for simple machined weld preparations [7].

A comprehensive volume inspection was conducted by TÜV Rheinland GmbH with CT scans of all welded specimens. Cracks, cavities, dimensions, lack of fusion, and penetration were examined and the findings were classified according to DIN EN ISO 6520-1. All results met the acceptance criteria.

Metallographic cuts were produced by cutting the specimens at the positions of the integrated features (the pins or bayonet

mounts). The highest risk of internal defects was expected to be found here due to increased surface roughness and gaps or void regions between the features. Insufficient purging with forming gas, exacerbated by the rough L-PBF surfaces, could have led to weld contamination with entrapped oxygen and increased pore development. In Figure 9, one metallographic cut is presented for each design, both non-welded (left) and welded (right). The metallographic cuts don't show any cracks, cavities, or lack of fusion or penetration. All internal features were completely dissolved in the melt pool. While occasionally small single pores with a diameter $<50\ \mu\text{m}$ were present, no larger pores or clustered porosity were detected. In the cuts, a visual distinction can be made between the root and top layer of the weld seam. The top layer excess was between 0.6 mm and 0.8 mm, and the root excess was between 0.5 mm and 1.1 mm for all measurements, fulfilling the criteria per DIN EN ISO 5817 for quality level B. The cross-section of the welded bayonet mount in Figure 9d shows a shifted cover layer, likely caused by a misalignment of the electrode. For serial production, the electrode alignment needs to be improved to ensure repeatable results.



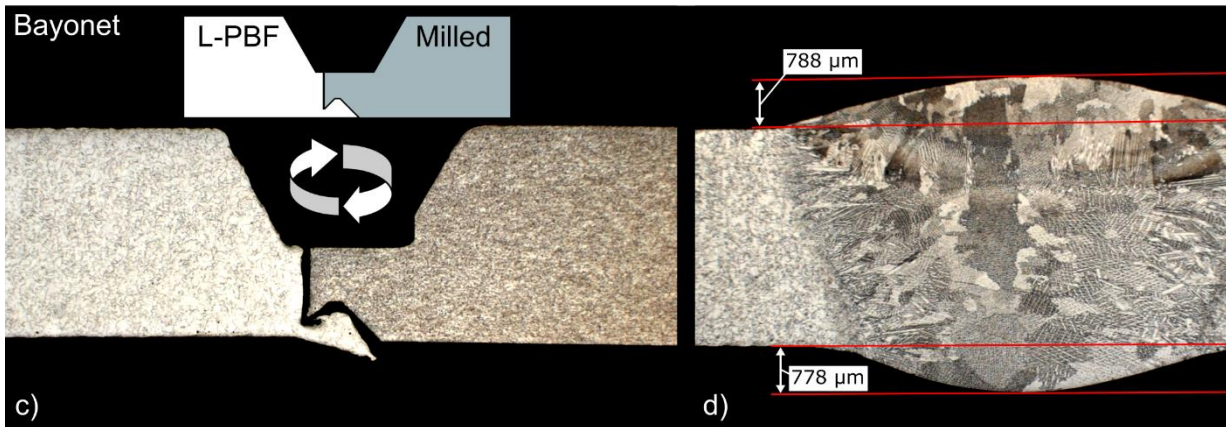


Figure 9: Metallographic cuts of the snap-fit joint in a) assembled and b) welded condition and of the bayonet joint in c) assembled and d) welded condition, including root penetration and cover excess measurements

Additional images of the heat affected zone (HAZ) of the snap-fit design are shown in Figure 10. The toes of the weld show sufficient overlap and a smooth transition to the base material. The change in a)

microstructure of the HAZ is more apparent in the fine-grained wrought material in Figure 10b), with a significant increase in grain size.

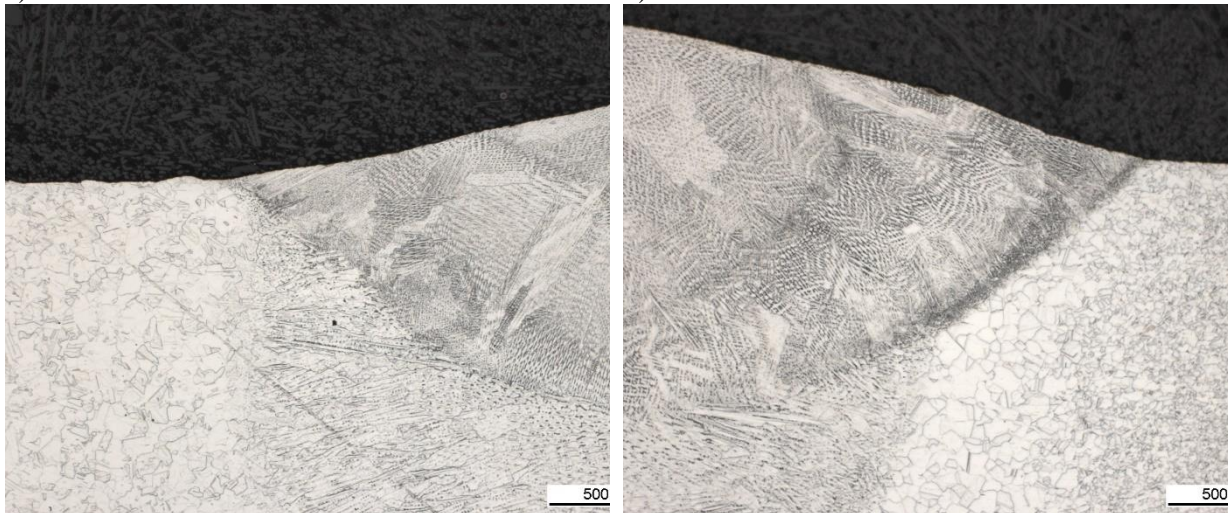


Figure 10: Details of the heat affected zone in the snap-fit joint, a) L-PBF material and b) wrought material

Figure 11 shows an EBSD image cut from the bayonet design. The grain sizes in the weld material are significantly larger compared to both the L-PBF and the conventional base material on the left and right sides respectively. Epitaxial grain growth can be observed at the fusion lines both between the base material and the root layer and between the root and the cover layer. These findings are in line with the

results from Geisen et al. [7], where increased grain sizes and epitaxial grain growth were also observed. The heat affected zone of the L-PBF material on the left side shows a less homogeneous grain size distribution compared to the conventional base material on the right side. As stated by Nguejio et al. [19] and Li et al. [20], this is a well-known difference between L-PBF and wrought material.

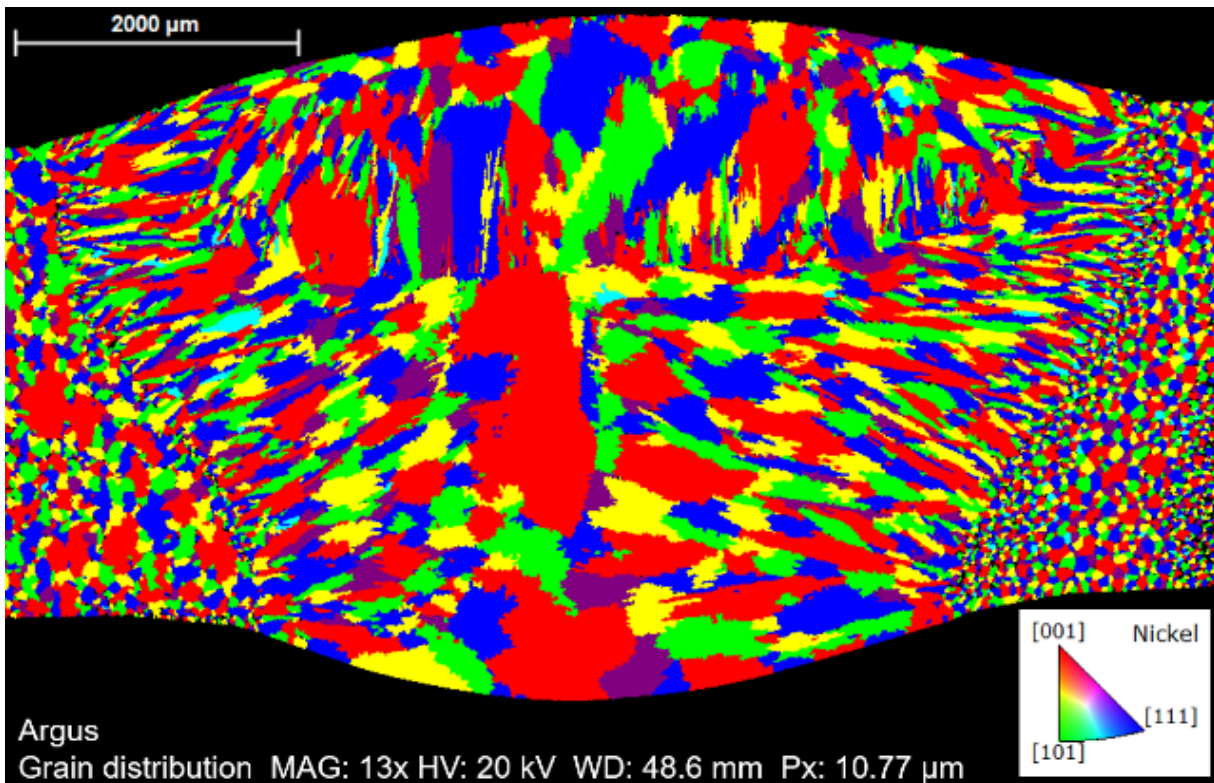


Figure 11: EBSD image of a weld seam with bayonet mount; L-PBF specimen on the left, milled specimen on the right.

In summary, no difference in weld joint quality could be detected between the two designs. All weld seams were free of significant external or internal defects. All integrated features were completely dissolved in the weld, and the root and cover excess dimensions were within tolerances. The weld quality per DIN EN ISO 5817 can be categorized in quality level B for all weld seams. This indicates that the welding parameters applied were suitable for the designs. It also proves adequate dimensioning of the integrated features and a balance between assembly functions and weldability.

6. Conclusion

The following conclusions can be drawn:

- Combining milling and L-PBF constraints in the weld preparation design is possible when using standard settings for both technologies.
- Multiple assembly mechanisms and design principles can be employed.
- Assembly of printed and milled parts meets requirements.
 - Positioning is within tolerances.
 - Fixation is safe for industrial environments and handling during production.
- Welding of the investigated designs meets quality requirements.
 - Quality level B, DIN 5187
 - Geometric accuracy is comparable to state-of-the-art weld preparation (subsequent heat straightening is necessary)
- Fixture-free production with no tack welds is possible, with the bayonet design showing the most robust results and the best potential for serial production, while the snap-fit design offers more design freedom and is applicable to non-symmetric parts.
- Manufacturing costs can be reduced with improved lead time, lower non-conformance costs, and elimination of fixture costs.

7. Summary

The successful integration of positioning and fixation into the part design, as demonstrated in this study, offers the opportunity to improve costs, lead time, and quality in the serial production of L-PBF parts in mixed joining setups. The solutions developed are applicable to all combustion systems in Siemens Energy gas turbines, because these components all have similar requirements and materials. In other industries like oil and gas, similar use cases with different materials and dimensions can be anticipated.

For future studies, we recommend that investigations be conducted on the mechanical properties of TIG welded specimens joining L-PBF to cast or wrought material. The designs should be investigated for their suitability for joining L-PBF to L-PBF components, and the impact of surface roughness on both parts should be studied. In addition, different materials and part dimensions can be analyzed. Finally, the transferability of the results to non-rotationally symmetric components can be studied to cover an even wider range of use cases.

8. References

1. AMPOWER Report (2020) Metal Additive Manufacturing: Management Summary
2. Gibson I, Rosen D, Stucker B (2015) Additive Manufacturing Technologies. Springer New York, New York, NY
3. Wits WW, Becker JJ (2015) Laser Beam Welding of Titanium Additive Manufactured Parts. *Procedia CIRP* 28:70–75. <https://doi.org/10.1016/j.procir.2015.04.013>
4. Casalino G, Campanelli SL, Ludovico AD (2013) Laser-arc hybrid welding of wrought to selective laser molten stainless steel. *Int J Adv Manuf Technol* 68:209–216. <https://doi.org/10.1007/s00170-012-4721-z>
5. Mäkikangas J, Rautio T, Mustakangas A et al. (2019) Laser Welding of AlSi10Mg Aluminium-based Alloy Produced by Selective Laser Melting (SLM). *Procedia Manufacturing* 36:88–94. <https://doi.org/10.1016/j.promfg.2019.08.013>
6. Jokisch T, Marko A, Gook S et al. (2019) Laser Welding of SLM-manufactured Tubes Made of IN625 and IN718. *Materials (Basel)* 12. <https://doi.org/10.3390/ma12182967>
7. Geisen O, Bogner J, Ghavampour E et al. (2020) Microstructure Analysis of Hybrid Laser Powder Bed Fusion and TIG Welding of Ni-based Superalloys. *enrXiv*. <https://doi.org/10.31224/osf.io/bz29t>
8. Klahn C, Singer D, Meboldt M (2016) Design Guidelines for Additive Manufactured Snap-Fit Joints. *Procedia CIRP*:264–269
9. Ramírez EA, Caicedo F, Hurel J et al. (2019) Methodology for design process of a snap-fit joint made by additive manufacturing. *Procedia CIRP* 79:113–118. <https://doi.org/10.1016/j.procir.2019.02.021>
10. International Organization for Standardization: ISO/ASTM 52910 (2018) Additive Manufacturing: Design, Requirements, Guidelines and Recommendations
11. International Organization for Standardization: ISO/ASTM 52911-2 (2017) Additive Manufacturing – Technical Design Guideline for Powder Bed Fusion - Part 2: Laser-based Powder Bed Fusion of Polymers

12. Fieger TV, Sattler MF, Witt G (2018) Developing Laser Beam Welding Parameters for the Assembly of Steel SLM Parts for the Automotive Industry. *Rapid Prototyping Journal*:1288–1295
13. Schwarz A, Gebhardt A, Schleser M et al. (2019) New Welding Joint Geometries Manufactured by Powder Bed Fusion from 316L. *Materials Performance and Characterization* 8:1249–1264.
<https://doi.org/10.1520/MPC20180096>
14. MTECK-Schweißtechnik GmbH (2021) Thermanit 625 Schweißdraht.
https://www.mteck-gmbh.de/schweisszusatzwerkstoffe/schweissdraht-fuer_alloy_617_2-4627_alloy_625_2-4831/thermanit_625/. Accessed 15 Feb 2021
15. VDM Metals (2021) Alloy 625.
<https://www.vdm-metals.com/de/alloy625/>. Accessed 15 Feb 2021
16. Fox JC, Moylan SP, Lane BM (2016) Effect of Process Parameters on the Surface Roughness of Overhanging Structures in Laser Powder Bed Fusion Additive Manufacturing. *Procedia CIRP* 45:131–134.
<https://doi.org/10.1016/j.procir.2016.02.347>
17. Sola A, Nouri A (2019) Microstructural Porosity in Additive Manufacturing: The Formation and Detection of Pores in Metal Parts Fabricated by Powder Bed Fusion. *Journal of Advanced Manufacturing and Processing*.
<https://doi.org/10.1002/amp2.10021>
18. Deutsches Institut für Normung e.V.: DIN EN ISO 5817:2014-06 (2014) Welding – Fusion-welded Joints in Steel, Nickel, Titanium and their Alloys (Beam Welding Excluded): Quality Levels for Imperfections, Berlin
19. Nguejio J, Szmytka F, Hallais S et al. (2019) Comparison of Microstructure Features and Mechanical Properties for Additive Manufactured and Wrought Nickel Alloys 625. *Materials Science and Engineering: A* 764.
<https://doi.org/10.1016/j.msea.2019.138214>
20. Li C, White R, Fang XY et al. (2017) Microstructure Evolution Characteristics of Inconel 625 Alloy from Selective Laser Melting to Heat Treatment. *Materials Science and Engineering: A* 705:20–31.
<https://doi.org/10.1016/j.msea.2017.08.058>